Direct drive or slider-crank? Comparing motor-actuated flapping-wing micro aerial vehicles

Moonsoo Park ⓘ **and Ali Abolfathi** ⓘ

Mechanical Engineering, University College London, London, United Kingdom

Corresponding author: **Ali Abolfathi** (email: a.abolfathi@ucl.ac.uk)

Abstract

For flapping-wing micro aerial vehicles, the common approach to converting the rotational motion of a DC motor to the reciprocal flapping motion is using a slider-crank mechanism. However, frictional losses in sliders and rotational joints can hinder the performance of such a system. An alternative is a direct drive system where the wings are directly connected to a DC motor that has been driven by an AC signal. These two approaches are compared in this paper, to evaluate their performances and assess which one provides a better solution for flapping-wing micro drones. The electromechanical model of the two systems is used in this paper to compare their performances. System parameters for both types of drones were derived through a multi-variable optimisation process using the same DC motor. The comparisons are made in terms of input power requirement, aerodynamic power, system efficiency, and lift. The direct drive model can generate about 16% higher average lift at 5 V with 50% lower input electrical power. It has 29% larger aerodynamic power and the system efficiency is 16.0% higher than that of the slider-crank model.

Key words: equations of motion, bioinspired flapping-wing micro aerial vehicle, FWMAV, kinetics of flapping mechanism, optimisation

1. Introduction

The electric motor is one of the most common actuators for flapping-wing micro aerial vehicles (FWMAVs). Its robustness, high power-to-weight ratio, ease of use, and low voltage operation make a motor well suited for FWMAVs (Keennon et al. 2012; Azhar et al. 2013). A review of motor-actuated FWMAVs is provided in Phan and Park (2019) and Xiao et al. (2021). FWMAVs driven by a motor typically require transmissions to convert the rotation to reciprocation and they increase the weight, power loss, and complexity of the system (Madangopal et al. 2005; Khan and Agrawal 2006; Tantanawat and Kota 2007; Baek et al. 2009; Azhar et al. 2013; Lau et al. 2014). To avoid the disadvantages, a direct drive concept is introduced (Campolo et al. 2012; Hines et al. 2013, 2015; Zhang and Rossi 2017; Pellerito and Vejdani 2019; Tu et al. 2020). It has been proved that both the slider-crank-based models and the direct drive models have the capability of hovering (Hines et al. 2015; Zhang and Rossi 2017). However, there is no research comparing those two systems. This paper aims to compare those two approaches in hover flight configuration.

A slider-crank mechanism (shown in Fig. 1a) is the simplest mechanical transmission converting rotating to reciprocal motion. Its dynamics are formulated and experimentally verified in Ha et al. (2006) and Erkaya et al. (2007). A slider-crank allows symmetrical flapping motions with a single rotary actuator. It is also easily modified by incorporating additional rods and adjusting the hinges as introduced in Zhang and

Rossi (2017) and Hassanalian and Abdelkefi (2019). A slider-crank mechanism leads to friction losses on the slider and hinges, which is important to model to estimate the energetic requirements correctly (Park et al. 2022).

A simpler system can be realised by driving the wings directly using a harmonic voltage (Campolo et al. 2012). The simple structure reduces the complexity of the system and allows structural robustness (Campolo et al. 2012). It is crucial for this system to include elastic components to reduce the effects of the high moment of inertia associated with the rotor, gears, and wing. The absence of these elastic elements results in a considerable increase in power input requirements, impeding the system's ability to achieve rapid reciprocating motion (Campolo et al. 2012). The inclusion of elastic elements effectively mitigates the inertia of both the motor and the wings (Azhar et al. 2013). Its reliable mathematical model is derived in Campolo et al. (2012) and Azhar et al. (2013), and its estimations are validated to the experimental data from their prototype with good accuracy.

The reciprocal motion of wings generates inertia loads that the actuator must counteract. Inertial loads are conservative forces and while the overall energy exchange for these forces in a cycle is zero, they can contribute to increased losses within the system e.g., due to increased internal forces (Park et al. 2022). Insects drive their wings at mechanical resonance to overcome this problem (Zhang et al. 2017). Elasticity in flight muscles, the thorax, and wing hinges enables them to

Fig. 1. Schematic view of (*a*) slider-crank model (Park et al. 2022) and (*b*) direct drive model. Lifts are generated along the *y* axis.
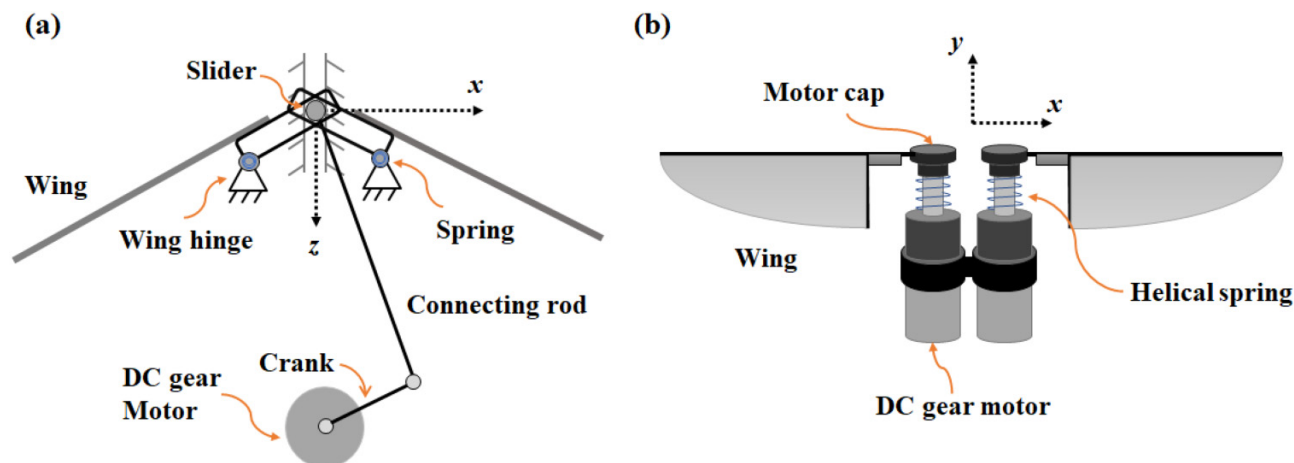
flap their wings at their natural frequency, allowing elastic forces to offset inertia forces within each cycle. It inspires researchers to utilise springs in FWMAVs to minimise the effect of inertial load and reduce losses. According to Madangopal et al. (2005), Tantanawat and Kota (2007), and Khan et al. (2009), incorporating springs on hinges in FWMAVs operated by a slider-crank mechanism is beneficial to reducing the motor torque variation and the maximum torque and input power requirement. Lau et al. (2014) built a compliant mechanism mimicking the thorax of a dipteran and showed that a compliant mechanism requires only 70%–80% of power expenditure from a rigid body model to generate the same amount of lift. Similarly, in the case of a motor direct drive system, helical springs are commonly incorporated on the shaft–wing connector to cancel out the effect of the inertial moment of the rotor. Azhar et al. (2013) show that a helical spring reduces the input power up to 16% at the resonance frequency. Campolo et al. (2012) experimentally added that incorporating a helical spring in the system allows larger wing motions, lower input power, and higher overall efficiency. Pellerito and Vejdani (2019) also numerically show that the spring between the wing and motor helps to generate a larger lift.

Although two competing mechanisms are studied and their models are developed, there is no systematic comparison of their performance to the best knowledge of the authors. This paper tries to fill this gap by providing a systematic comparison of the two systems. A commercially available mini motor is chosen to develop the flapping systems where the parameters are optimised to obtain maximum lift and energy efficiency in the hovering flight condition. MATLAB Simulink is used here for numerical simulations. A general comparison of both concepts is provided in Section 2. The mathematical models for both flapping systems are presented in Section 3, and the average powers and efficiencies that are used for the comparisons are defined in Section 4. The optimum values of each system are determined in Section 5 and the performances of the two systems are compared in Section 6.

2. Flapping-wing systems

The slider-crank mechanism is one of the most traditional transmissions for motor-driven flapping mechanisms, while the direct drive model is a relatively new approach thanks to the development of power electronics. The schematic views for a slider–crank-based model (Lau et al. 2014) and the direct drive model (Azhar et al. 2013) are illustrated in Figs. 1*a* and 1*b*, respectively.

Since the actuator is the heaviest component among the parts in the system, the slider-crank model tends to be lighter than the direct drive model that has two actuators (Campolo 2010; Campolo et al. 2012; Lau et al. 2014; Akbari et al. 2016). However, the slider-crank model is larger due to the space for rods and supporting structures enabling reciprocation. The slider–crank mechanism has intrinsic nonlinearity in the inertia term, which leads to nonsinusoidal profiles of wing stroke and torque on wing hinges. When used alongside linear springs, the nonlinearity makes it difficult to compensate for inertia loads fully (Baek et al. 2009). For the direct drive system, the wing beat can be assumed as a quasi-sinusoidal motion when the input is sinusoidal, which is beneficial to utilise elastic energy effectively (Campolo et al. 2012). In this case, aerodynamic forces are the dominant source of nonlinearity in the system. When it comes to the losses, friction on the slider and rotational hinges results in increased power losses in the slider-crank system while there is no sliding part in the direct drive and the losses can be limited to the electromechanical losses of the gear-motor.

Motors experience rapidly changing loads in both flapping-wing systems. The main difference between the two models is that the rotor of the motor in the slider-crank model continuously rotates in one direction, while the one in the direct drive model reciprocates. Springs in the slider-crank model mitigate the oscillation of the wing inertial load so that the motor can operate at a relatively stable load. Similarly, in the direct drive model, tuned springs compensate for the effect of the inertial moment of the rotor and the wing. Although springs are advantageous to both systems, the resonance is

Table 1. Simulation parameters for the DC motor.

Parameter	Input value
R_a	$9\ \Omega$
L_a	$29\ \text{mH}$
K_b	$10\ \text{mNm/A}$
J_m	$1.5 \times 10^{-7}\ \text{kgm}^2$
b_m	$3.6 \times 10^{-6}\ \text{Ns/rad}$

utilised more effectively in the direct drive system. Thus, the reciprocation can be generated with less input power in the direct drive system as can be seen in the efficiency analysis provided in Section 6.

3. Modelling

The mathematical models are provided here for the motor, wings, slider-crank mechanism, and direct drive systems. A geared DC motor is modelled using the characteristic equations of a DC motor. Quarter ellipse-shaped wings are introduced, taking into account their mechanical properties and passive rotation. The integrations of these two parts are performed while taking into account the kinematic movement of the mechanisms within each system.

3.1. Motor

The characteristic equations of a DC motor are (Craig 2006)

$$(1) \qquad v = L_a \frac{\mathrm{d}i}{\mathrm{d}t} + R_a i + e_{\text{EMF}}$$

$$(2) \qquad T_m - T_L = J_m \ddot{\theta}_m + b_m \dot{\theta}_m$$

$$(3) \qquad T_m = K_t i$$

$$(4) \qquad e_{\text{EMF}} = K_t \dot{\theta}_m$$

where v is the applied voltage, i is the armature current, R_a is the armature coil resistance, L_a is the armature coil inductance, e_{EMF} is the back electromotive force, T_m is the motor output torque, T_L is the load torque, J_m is the motor inertia, $\dot{\theta}_m$ is the motor shaft speed, K_t is the motor torque constant, and b_m is the mechanical loss coefficient of the motor.

A commercial DC motor (206-102 by Precision Microdrives Ltd) was selected as the actuator in this study and its characteristics are summarised in Table 1.

3.2. Wings

Using the blade element method, the resultant aerodynamic lift, L_r, and drag, D_r, acting on a sectional area A_r at a distance r from the wing hinge are defined as (Pornsin-Sirirak et al. 2001)

$$(5) \qquad L_r = \frac{1}{2}\rho V_r^2 A_r C_L$$

$$(6) \qquad D_r = \frac{1}{2}\rho V_r |V_r| A_r C_D$$

$$(7) \qquad A_r = c(r)\,\mathrm{d}r$$

where ρ is the air density, V_r is the relative air velocity, C_L and C_D are the lift and drag coefficients, respectively, and $c(r)$ is the chord length at r.

It is assumed that the shape of the wing is a quarter ellipse and the cross-sectional areas of the frames are constant to make the calculation simple. The geometry of the wings and the directions of the lift and drag on the flapping wing are illustrated in Fig. 2. The wing is assumed to undergo passive rotation, reducing the angle of attack to α from an angle of $90°$. This study is conducted on the premise that the systems operate in a hover configuration, with gravity acting along the y axis.

The lift and drag coefficients due to the translational motion are obtained by Dickinson et al. (1999) as functions of the instantaneous angle of attack, α in radian

$$(8) \qquad C_L = 0.225 + 1.58 \times \sin(2.13\alpha - 0.1257)$$

$$(9) \qquad C_D = 1.92 - 1.55 \times \cos(2.04\alpha - 0.1714)$$

A flexible wing root chord facilitates passive rotation in accordance with the wing stroke motions. The angle of attack can be assumed to be a function of the wing angular velocity, $\dot{\beta}$ (Park et al. 2022)

$$(10) \qquad \alpha = \frac{\pi}{2} - C_\alpha \left|\dot{\beta}\right|$$

where C_α is an arbitrary coefficient that is empirically obtained and is equivalent to 5×10^{-3} (Park et al. 2022). In this study, C_α is postulated to remain constant regardless of the wing size and α is limited to a minimum of $\pi/4$. The limit is considered to avoid very large deformation. Such a limit can be achieved by an appropriate design of the wings and increasing C_α, which is beyond the scope of this paper.

The distance of the wing aerodynamic centre from the wing hinge can be calculated from

$$(11) \qquad \bar{r} = \frac{\int_{\frac{L_b}{2}}^{L_e + L_b/2} D_r r\,\mathrm{d}r}{\int_{\frac{L_b}{2}}^{L_e + L_b/2} D_r\,\mathrm{d}r}$$

The mass moment of inertia of the wing is

$$(12) \qquad J_w = \frac{1}{3}A_{wb}L_b^3\rho_{wf} + \frac{1}{3}A_{wf}L_e\rho_{wf}\left(L_e + \frac{L_b}{2}\right)^2$$
$$+ \frac{1}{3}A_{wf}L_c\rho_{wf}\left(\frac{L_b}{2}\right)^2 + \frac{\pi}{4}L_c L_w t_{mb}\rho_{mb} \times \bar{r}^2$$

where A_{wb} is the cross-sectional area of the wing base, A_{wf} is the cross-sectional area of the wing frame ($1\ \text{mm}^2$), t_{mb} is the thickness of the membrane, ρ_{wf} is the mass density of the wing frame ($1900\ \text{kg/m}^3$), ρ_{mb} is the mass density of the membrane ($1100\ \text{kg/m}^3$), and the ratio of L_e/L_c is defined as the aspect ratio of the wing. The wing materials are assumed to be the same as the wing introduced in Lau et al. (2014). The frames are made of carbon fibre reinforced polymer (CFRP) and the membranes are fabricated from polyimide film (Dupont Kapton HN). The wing base is made of CFRP and its size is fixed to be $10\ \text{mm} \times 5\ \text{mm} \times 1\ \text{mm}$.

Fig. 2. (*a*) The geometry and profile of the wing and (*b*) the cross-section of the wing showing the force components on a flapping wing, where *y* is the rotational axis for the wing and lift is generated along the *y* axis.
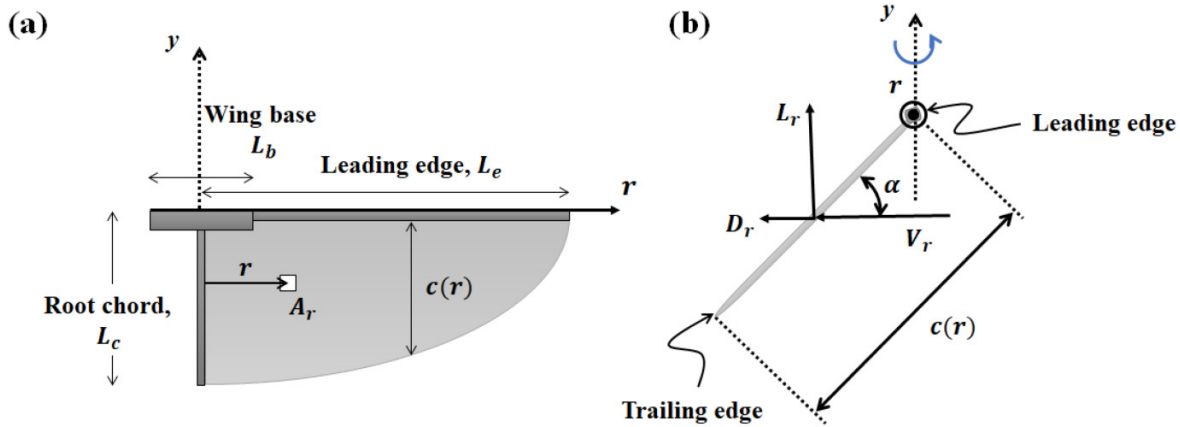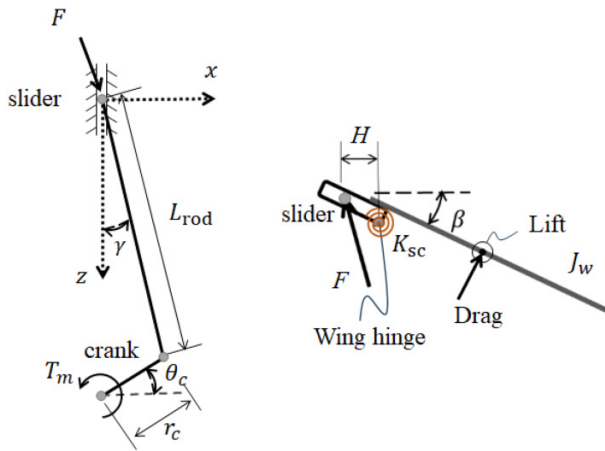

Fig. 3. The free body diagram of the slider-crank mechanism showing crank reaction force, *F*, and motor torque, T_m.

3.3. Slider-crank model

The free-body diagram of the slider-crank mechanism and wing is depicted in Fig. 3.

By neglecting the inertial moment of the connecting rod and the crankshaft, the equation of motion for the slider-crank system can be obtained (Park et al. 2022)

(13) $\quad J_w \ddot{\beta} + C_w \dot{\beta} |\dot{\beta}| + K_{SC}\beta = FH(\sin\gamma \tan\beta + \cos\gamma)$

where F is the crank reaction force, H is the horizontal distance between the wing hinge and the slider, β is the wing stroke angle with the horizontal axis, γ is the angle between the connecting rod and the vertical axis, K_{SC} is stiffness of spring on the wing hinge, and C_w is the aerodynamic damping coefficient obtained from the following equation:

(14) $\quad C_w = C_D(\alpha_e) \int_0^r \frac{1}{2}\rho r^3 A_r \mathrm{d}r$

The stiffness of the springs added to the hinges, K_{sc}, can be obtained by choosing an arbitrary resonant frequency ω_{nw} for the wing–spring system,

(15) $\quad K_{SC} = J_w \omega_{nw}^2$

The crank reaction force can be obtained using the motor torque

(16) $\quad T_m - T_f = Fr_c(\sin\theta_c \sin\gamma + \cos\theta_c \cos\gamma)$

where T_m is the motor output torque, T_f is the equivalent torque due to friction losses in the system called friction torque here, r_c is the crank radius, θ_c is the angle between the crank arm and the horizontal axis, and γ is the angle between the connecting rod, L_{rod}, and the vertical axis. To obtain the friction torque, T_f, as a function of internal loads, the Coulomb friction model is used (Park et al. 2022)

(17) $\quad T_f = F\mu r_e$

where μ is the friction coefficient and r_e is the effective radius. The product μr_e is estimated to be 2.5×10^{-3} using experimental data in Lau et al. (2014).

3.4. Direct-drive model

The equation of motion can be represented as the second-order differential equation by combining the mechanical properties into the motor eqs. 1–4 (Campolo 2010; Campolo et al. 2012; Azhar et al. 2013). The overall system can be described as

(18) $\quad T_m = (J_w + J_m)\ddot{\beta} + b_m\dot{\beta} + C_w\dot{\beta}|\dot{\beta}| + K_{DD}\beta$

The spring constant of the helical spring attached to the wing and shaft is set equal to

(19) $\quad K_{DD} = (J_m + J_w)\omega_{DD}^2$

where ω_{DD} is the intended wingbeat frequency of the direct-drive system.

4. Power and efficiencies

The average electrical input power, P_e, and the motor output power, P_m, can be obtained from the following equations:

(20) $\quad P_e = \frac{1}{T}\int_T vi\mathrm{d}t$

(21) $\quad P_m = \frac{1}{T}\int_T |T_m\dot{\theta}|\mathrm{d}t$

where T is the period of the wing stroke in a steady state.

The aerodynamic power from the slider-crank model and the direct drive models are defined as

$$(22) \quad P_{a} = \frac{1}{T} \int_{T} \left(\bar{D}\bar{r} \right) \dot{\beta} \mathrm{d}t$$

This study focuses on the performance of FWMAVs in hovering, where lift is crucial for keeping vehicles airborne. Averaging the aerodynamic forces in a cycle, the average lift generated significantly outweighs the average drag force, making the latter negligible and noncontributory to the hovering flight. Nevertheless, drag can be considered as the cost to produce lift (Alexander 2015) and hence the efficiency of the system, η_s, can be defined as

$$(23) \quad \eta_{s} = \frac{P_{a}}{P_{e}} \times 100$$

5. Optimisations

The same DC motor as described in Section 3.1 is used here to compare the performance of the two systems. To compare the best possible performance of two flapping mechanisms with the same motor, system parameters are optimised using numerical simulations. The mathematical models were implemented in MATLAB and Simulink and were used to obtain the response of the systems. The average powers and forces are calculated using one cycle after the systems reach the steady state condition.

A multi-parameter optimisation approach is employed here using MATLAB's "fmincon" function and the average lift serves as the optimisation indicator. The optimisation aims to find the combination of the design parameters that produces the maximum average lift at 3 and 5 V, which are the rated voltage and the maximum voltage that the motor can endure for a finite duration, respectively (Lau et al. 2014). For the slider-crank system, the following parameters are considered design parameters: the length of the wing leading edge, L_e, stiffness of the spring, K_{SC}, crank length, r_c, connecting rod length, L_{rod}, and the length between the slider and wing hinge, H. For the direct drive system, the length of the wing leading edge, L_e, stiffness of the spring, K_{DD}, and the frequency of the input voltage are considered as design variables.

Equations 8 and 9 are obtained by mimicking Drosophila's wings (Dickinson et al. 1999). Earlier studies on Drosophila have reported aspect ratios in the range of 2.91–3.14 (Ennos 1989; Zanker 1990). To employ the empirically determined lift and drag coefficients, the aspect ratio is considered fixed here and equal to 3. To determine the wing properties, the length of the wing's leading edge is set to be a design variable of the wing, while other wing parameters are proportionally changed by the length. The optimum variables for the slider-crank model and direct drive model are given in Tables 2 and 3, respectively.

6. System comparisons

The comparative analysis focused on several key parameters: average input power, average aerodynamic power, sys-

Table 2. Optimal system specifications for slider-crank (SC) model.

Parameters	SC model		Units
$\bar{v}$	3	5	V
$\bar{f_o}$	25.28	41.88	Hz
L_e	52.34	54.01	mm
K_{SC}	4.49	8.10	mNm/rad
r_c	8.59	9.47	mm
L_{rod}	20.0	21.0	mm
H	10.24	11.73	mm

Note: $\bar{v}$ is the voltage used to find optimum values and $\bar{f_o}$ is the optimal frequency of the system.

Table 3. Optimal system specifications for direct drive (DD) model.

Parameters	DD model		Units
$\bar{v}$	3	5	V
$\bar{f_o}$	35.67	23.89	Hz
L_e	60.49	68.46	mm
K_{DD}	15.80	8.65	mNm/rad

Note: $\bar{v}$ is the voltage used to find optimum values and $\bar{f_o}$ is the optimal frequency of the system.

tem efficiency, and average lift. This analysis is conducted using the optimum design variables described in Tables 2 and 3. The performance of the direct drive model is estimated from a single motor to achieve a fair comparison. To investigate the average lift and efficiency over a wider operating frequency range, the graphs are plotted with various inputs. For the slider-crank model, the input voltage varies from the minimum voltage required to operate the system up to 3 and 5 V. The amplitude of the input voltage to the direct drive model is fixed at 3 and 5 V, while its frequency varies from 15 to 45 Hz. The comparisons between two models are graphically represented in Fig. 4 and its summary is described in Table 4.

The maximum average lifts of the slider-crank system, 10.10 mN at 3 V and 27.11 mN at 5 V, are 17.95% at 3 V and 16.20% at 5 V lower than that of the direct drive system (12.31 mN at 3 V, 35.67 Hz and 32.35 mN at 5 V, 23.89 Hz). The maximum efficiency of the direct drive system is more than twice as high as that of the slider–crank one. The maximum efficiency of the slider-crank model is about 14.17% and 13.84% at 3 and 5 V, respectively while the maximum efficiency of around 33.74% and 29.87% are achieved in the direct drive system at 3 V, 35.67 Hz and at 5 V, 23.89 Hz, respectively. When it comes to powers, the slider-crank system exhibits about 24.42% lower aerodynamic power and around 83.98% higher input power than the direct drive system when operated at 3 V. At 5 V, the slider–crank model generates approximately 29.0% lower aerodynamic power from about 50.0% higher input power compared to the direct drive model.

Wing stroke angle is a distinguishing characteristic of the two systems. The stroke angles observed in two systems with

Fig. 4. (*a*) Average lift, (*b*) system efficiency, (*c*) average electrical input powers, and (*d*) average aerodynamic powers as a function of frequency for the slider-crank drive and direct drive systems. DD: direct drive system, utilising data by considering a single motor of the DD model; SC: slider-crank system; blue and red lines: slider-crank system optimised at 3 and 5 V; yellow and green lines: direct drive system optimised at 3 and 5 V.
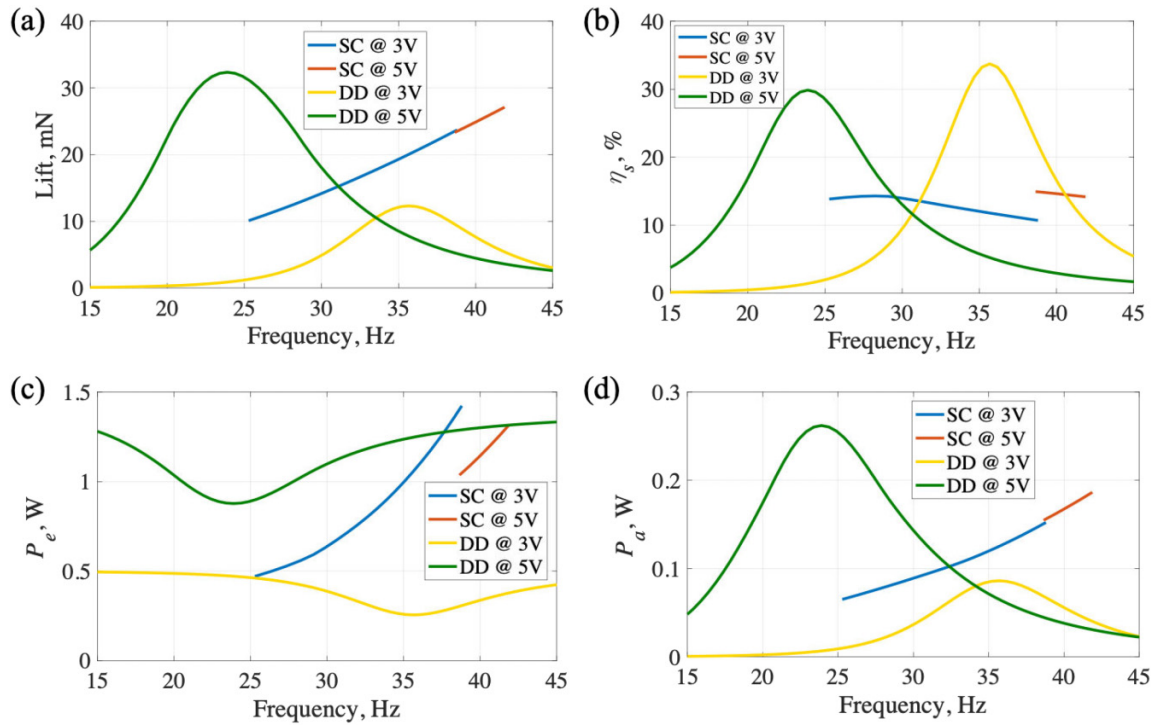

Table 4. Comparisons between slider-crank (SC) and direct drive (DD) models under different optimised conditions, utilising data by considering a single motor of the DD model.

Parameters	SC model		DD model		Units
$\bar{v}$	3	5	3	5	V
$\bar{f_o}$	25.28	41.88	35.67	23.89	Hz
Operating range	3–5 V_{DC}	4.5–5 V_{DC}	3 V, 15–45 Hz	5 V, 15–45 Hz	–
Max. average lift	10.10	27.11	12.31	32.35	mN
Max. η_s	13.84	14.17	33.74	29.87	%
Avg. P_e	0.471	1.316	0.256	0.877	W
Avg. P_a	0.065	0.186	0.086	0.262	W
Max. β at $\bar{f_o}$	77.7	77.8	75.00	140.64	°

Note: $\bar{v}$ is the voltage amplitude used to find optimum values and $\bar{f_o}$ is the optimal frequency of the system.

the optimum variables are compared in Fig. 5 and the maximum stroke angles are described in Table 4. The stroke angle of the slider-crank model is determined by the geometry of the slider-crank mechanism and is fixed while it varies by the input voltage and the wing load in the direct drive model. In the direct drive model, the stroke angle is maximised near the resonant frequency of the spring whereas the springs act as extra loads if the system runs below the resonant frequency.

To sum up, the direct drive model exhibits enhanced performance characteristics compared to the slider-crank model. The direct drive model requires less input power to generate a greater amount of aerodynamic power and average lift, thereby resulting in higher system efficiency. This superiority in performance can be attributed to the absence of nonlinearity in the flapping mechanism and lower energy loss due to the absence of sliding components.

7. Conclusions

The performances of flapping-wing systems using motor drive slider-crank and direct drive concepts are compared in this study. Visible characteristics are summarised and mathematical models are provided. The wing shape is assumed to be a quarter ellipse and its dimensions are optimised to form a flapping-wing drone using the same commercially available

6

Drone Syst. Appl. **12:** 1–8 (2024) | dx.doi.org/10.1139/dsa-2023-0026

Fig. 5. Wing stroke angle along the operating frequency at the input voltage of 3 and 5 V. Blue solid and red dashed lines are for the slider-crank (SC) system optimised at 3 and 5 V, respectively; yellow and green solid lines are for the direct drive (DD) system optimised at 3 and 5 V, respectively.
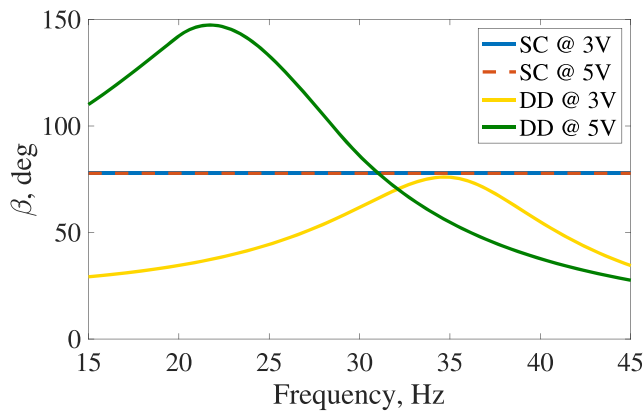
geared DC motor. The optimum sizes of the wings are determined for both cases to compare the two systems when they are producing the maximum possible lift. The system comparisons are made in terms of the average input power, aerodynamic power, lift, and system efficiency.

The mechanical losses of the slider-crank mechanism are modelled as the equivalent friction losses of the motor rotational hinge, while the losses of the direct drive system are modelled as the motor losses only. Although two motors are used in the direct drive flapping system, only one of them is considered here to provide an assessment based on a single motor for both cases. Thus, half of the power and half of the lift of the direct drive system are compared to the entire power and lift of the slider-crank mechanism. At the motor's rated voltage of 3 V, the slider-crank system can generate about 17.95% lower average lift, produce approximately 24.42% lower aerodynamic power, and require approximately 83.98% higher input power, leading to 19.57% lower efficiency. At the motor's maximum input voltage of 5 V, the slider–crank flyer can generate approximately 16.20% lower average lift with 29.0% lower aerodynamic power. It needs 50.0% larger input electrical power and has 16.03% lower efficiency compared to the direct drive model. The main benefits of the direct drive model result from the effective cancellation of the inertial loads, the reduced frictional losses, and the controllability of the frequency of the system. The model can achieve various outputs at the same frequency. The disadvantage of the direct drive model is the narrow driving frequency range. At different frequencies to the natural frequency of the system, the performance of the system is dramatically degraded.

Losses in the slider-crank mechanism are derived from a prior study (Park et al. 2022) and are based on a single prototype. While the use of advanced materials and manufacturing methods may lead to reduced losses in a slider-crank mechanism, the presence of sliding motion will consistently result in higher losses compared to the direct drive model. Furthermore, empirical data are employed for a specific wing shape

and motor. Given that the same wing shape is used for both systems, it is improbable that altering the wing shape would significantly impact the conclusions of this paper. However, different values for lift and efficiency may be obtained by using different wing models and motors.

Article information

History dates

Copyright

Data availability

Author information

Author ORCIDs
Moonsoo Park https://orcid.org/0000-0001-6165-5295
Ali Abolfathi https://orcid.org/0000-0003-0584-4758

Author contributions
Conceptualization: AA
Formal analysis: MP
Methodology: MP, AA
Software: MP
Supervision: AA
Writing – original draft: MP
Writing – review & editing: AA

Competing interests
The authors declare there are no competing interests.

Funding information

References

Akbari, S., Fallahi, F., and Pirbodaghi, T. 2016. Dynamic analysis and controller design for a slider-crank mechanism with piezoelectric actuators. J. Comput. Des. Eng. **3**(4): 312–321. doi:10.1016/j.jcde.2016.05.002.

Alexander, D.E. 2015. On the wing: insects, pterosaurs, birds, bats and the evolution of animal flight. Oxford University Press, USA.

Azhar, M., Campolo, D., Lau, G.K., Hines, L., and Sitti, M. 2013. Flapping wings via direct-driving by DC motors. *In* 2013 IEEE Interna-

tional Conference on Robotics and Automation. IEEE.pp. 1397–1402. doi:10.1109/ICRA.2013.6630753.

Baek, S.S., Ma, K.Y., and Fearing, R.S. 2009. Efficient resonant drive of flapping-wing robots. *In* 2009 IEEE/RSJ International Conference on Intelligent Robots and Systems. IEEE.pp. 2854–2860. doi:10.1109/IROS.2009.5354725.

Campolo, D. 2010. Motor selection via impedance-matching for driving nonlinearly damped, resonant loads. Mechatronics, **20**(5): 566–573. doi:10.1016/j.mechatronics.2010.05.008.

Campolo, D., Azhar, M., Lau, G.K., and Sitti, M. 2012. Can DC motors directly drive flapping wings at high frequency and large wing strokes? IEEE/ASME Trans. Mechatron. **19**(1): 109–120. doi:10.1109/TMECH.2012.2222432.

Craig, J.J. 2006. Introduction to robotics. Pearson Education.

Dickinson, M.H., Lehmann, F.O., and Sane, S.P. 1999. Wing rotation and the aerodynamic basis of insect flight. Science, **284**(5422): 1954–1960. doi:10.1126/science.284.5422.1954. PMID: 10373107.

Ennos, A.R. 1989. The effect of size on the optimal shapes of gliding insects and seeds. Journal of Zoology, **219**(1): 61–69. doi:10.1111/j.1469-7998.1989.tb02565.x.

Erkaya, S., Su, Ş., and Uzmay, I. 2007. Dynamic analysis of a slider-crank mechanism with eccentric connector and planetary gears. Mech. Mach. Theory, **42**(4): 393–408. doi:10.1016/j.mechmachtheory.2006.04.011.

Ha, J.L., Fung, R.F., Chen, K.Y., and Hsien, S.C. 2006. Dynamic modeling and identification of a slider-crank mechanism. J. Sound Vib. **289**(4–5): 1019–1044. doi:10.1016/j.jsv.2005.03.011.

Hassanalian, M., and Abdelkefi, A. 2019. Towards improved hybrid actuation mechanisms for flapping wing micro air vehicles: analytical and experimental investigations. Drones, **3**(3): 73. doi:10.3390/drones3030073.

Hines, L., Campolo, D., and Sitti, M. 2013. Liftoff of a motor-driven, flapping-wing microaerial vehicle capable of resonance. IEEE Trans. Robot. **30**(1): 220–232. doi:10.1109/TRO.2013.2280057.

Hines, L., Colmenares, D., and Sitti, M. 2015. Platform design and tethered flight of a motor-driven flapping-wing system. *In* 2015 IEEE International Conference on Robotics and Automation (ICRA). IEEE. pp. 5838–5845. doi:10.1109/ICRA.2015.7140016.

Keennon, M., Klingebiel, K., and Won, H. 2012. Development of the nano hummingbird: a tailless flapping wing micro air vehicle. *In* 50th AIAA Aerospace Sciences Meeting including the New Horizons Forum and Aerospace Exposition. p. 588. doi:10.2514/6.2012-588.

Khan, Z., Steelman, K., and Agrawal, S. 2009. Development of insect thorax based flapping mechanism. *In* 2009 IEEE International Conference on Robotics and Automation. IEEE. pp. 3651–3656. doi:10.1109/ROBOT.2009.5152822.

Khan, Z.A., and Agrawal, S.K., 2006. Design of flapping mechanisms based on transverse bending phenomena in insects. *In* Proceedings

2006 IEEE International Conference on Robotics and Automation, 2006. ICRA 2006. IEEE.pp. 323–2328. doi:10.1109/ROBOT.2006.1642049.

Lau, G.K., Chin, Y.W., Goh, J.T.W., and Wood, R.J. 2014. Dipteran-insect-inspired thoracic mechanism with nonlinear stiffness to save inertial power of flapping-wing flight. IEEE Trans. Robot. **30**(5): 1187–1197. doi:10.1109/TRO.2014.2333112.

Madangopal, R., Khan, Z.A., and Agrawal, S.K. 2005. Biologically inspired design of small flapping wing air vehicles using four-bar mechanisms and quasi-steady aerodynamics. J. Mech. Des. **127**(4): 809–816. doi:10.1115/1.1899690.

Park, M., Ventikos, Y., and Abolfathi, A. 2022. Should friction losses be included in an electromechanical model of a bioinspired flapping-wing micro aerial vehicle to estimate the flight energetic requirements? Bioinspiration Biomimetics, **17**(3): 036011. doi:10.1088/1748-3190/ac59c4.

Pellerito, V., and Vejdani, H. 2019. The effect of wing-motor connection mechanism on the payload capacity of flapping flight hovering robots. *In* Dynamic Systems and Control Conference. Vol. 59155. p. V002T25A006. doi:10.1115/DSCC2019-9203.

Phan, H.V., and Park, H.C. 2019. Insect-inspired, tailless, hover-capable flapping-wing robots: recent progress, challenges, and future directions. Progr. Aerosp. Sci. **111**. 100573. doi:10.1016/j.paerosci.2019.100573.

Pornsin-Sirirak, T.N., Tai, Y.C., Ho, C.M., and Keennon, M. 2001. Microbat: a palm-sized electrically powered ornithopter. *In* Proceedings of NASA/JPL Workshop on Biomorphic Robotics. Vol. 14. p. 17.

Tantanawat, T., and Kota, S. 2007. Design of compliant mechanisms for minimizing input power in dynamic applications. J. Mech. Des. **129**(10): 1064–1075. doi:10.1115/DETC2006-99430.

Tu, Z., Fei, F., and Deng, X. 2020. Untethered flight of an at-scale dual-motor hummingbird robot with bio-inspired decoupled wings. IEEE Robot. Autom. Lett. **5**(3): 4194–4201. doi:10.1109/LRA.2020.2974717.

Xiao, S., Hu, K., Huang, B., Deng, H., and Ding, X. 2021. A review of research on the mechanical design of hoverable flapping wing micro-air vehicles. J. Bionic Eng. **18**. 1235–1254. doi:10.1007/s42235-021-00118-4.

Zanker, J. M. 1990. The wing beat of Drosophila Melanogaster. I. Kinematics. Phil. Trans. R. Soc. Lond. B **327**: 1–18. doi:10.1098/rstb.1990.0040

Zhang, C., and Rossi, C. 2017. A review of compliant transmission mechanisms for bio-inspired flapping-wing micro air vehicles. Bioinspiration Biomimetics, **12**(2): 025005. doi:10.1088/1748-3190/aa58d3.

Zhang, J., Fei, F., Tu, Z., and Deng, X. 2017. Design optimization and system integration of robotic hummingbird. *In* 2017 IEEE International Conference on Robotics and Automation (ICRA). pp. 5422–5428. doi:10.1109/ICRA.2017.7989639.